Instantaneous Pulse Pattern Control of Three-Phase Multi-Active Bridge DC-DC Converters

Jonghun Yun, Jaekeun Lee, Giovanni De Carne, Shenghui Cui

***Abstract*—A three-phase multi-active bridge (MAB3) converter is a multiport dc-dc converter for high power applications. Its three-phase multi-winding transformer enables flexible power flow between multiple dc sources, offering superior high power density and efficiency. However, when fixed duty cycles are employed with mismatched dc voltage conditions, the efficiency of the MAB3 deteriorates, particularly in light-load conditions. To address this, modulation schemes with variable duty cycles are needed, along with dynamic control. However, few studies have explored dynamic control methods compatible with such multi-variable modulations. Without proper dynamic control, step changes in voltage patterns can induce transient overcurrents and transformer flux saturation, limiting the achievable power slew rate. Consequently, mitigating this poor dynamic performance may necessitate transformer overdesign or larger DC-link capacitance. To overcome these challenges, this article proposes an instantaneous pulse pattern control (IPPC) to support generic modulations of MAB3 converters. By formulating dynamic control as a multi-flux regulation problem, the IPPC enables to accommodate the generic modulation schemes while achieving consistent and minimized transient times. Experimental results demonstrate that the proposed IPPC consistently reduces transient times to a single sampling period, equivalent to one sixth of the switching period.**

***Index Terms*—Multi-active bridge, dynamic control, variable duty cycle, flux regulation.**

I. Introduction

With the rising demand for multiple dc sources in power systems, increasing attention has been directed toward multi-active bridge (MAB) converters [1]–[6]. The MAB converter extends the dual-active bridge (DAB) topology by integrating multiple active bridges through a single multi-winding transformer. This configuration facilitates flexible power flow control while reducing the number of power conversion stages and system components compared to systems using multiple DAB converters. As illustrated in Fig. 1, the MAB replaces numerous two-port transformers into a single multi-winding transformer, thereby enhancing power density and overall efficiency.

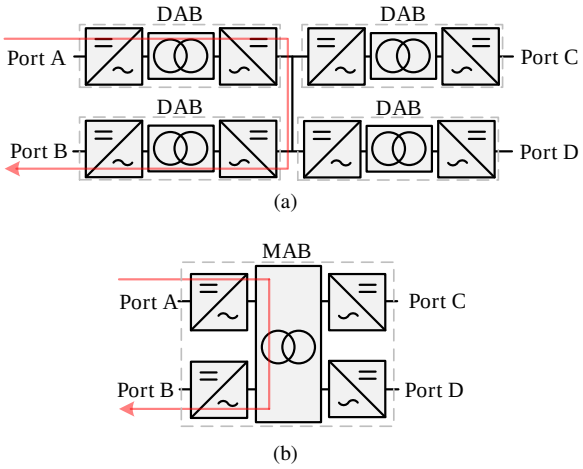

Fig. 1. Multiport system structures based on (a) multiple DAB converters (b) and a single MAB converter.

For high-power applications where the volume of passive components becomes significant, a three-phase configuration offers advantages for MAB converters over their single-phase counterparts. In the case of the DAB converter, which is the foundational topology of the MAB, it is known that the three-phase configuration substantially reduce the volume of the dc-link filter capacitor and medium-frequency transformer (MFT). Since the three-phase DAB exhibits a capacitor ripple current frequency three times higher than its single-phase counterpart, the filter capacitor volume can be reduced [7]–[9]. In addition, as the three-phase MFT transformer benefits from the flux cancellation effect and lower rms current, its volume also can be reduced compared to a single-phase MFT [10]–[12].

These characteristics extend to the three-phase multi-active bridge (MAB3) converter. Since a multiport configuration also reduces the volume of passive components, by reducing the number of transformers and dc-link capacitors, the integration of the three-phase topology with the multiport configuration offers a significant potential to maximizing power density, compared to using a single-phase MAB or multiple three-phase DABs for high-power multiport applications. [13]–[15].

Single phase-shift (SPS) modulation is currently the most widely adopted method for power flow control of MAB3

Manuscript received 13 August 2025; revised 29 November 2025; revised 28 January 2026; accepted 26 February 2026. This work was supported in part by the Technology Innovation Program (or Industrial Strategic Technology Development Program under Grant RS-2024-00432085, Development of Control System for High Power Medium-Voltage Drive based on Modular Multilevel Converter) funded by the Ministry of Trade, Industry and Energy (MOTIE, South Korea), and in part by the Korea Institute of Energy Technology Evaluation and Planning (KETEP) through the Ministry of Climate, Energy and Environment (MCEE) under Grant 20224000000160 (DC Grid Energy Innovation Research Center). (Corresponding author: *Shenghui Cui*.)

Jonghun Yun and Giovanni De Carne are with the Institute of Technical Physics, Karlsruhe Institute of Technology, 76131 Karlsruhe, Germany (e-mail: jonghun.yun@kit.edu; giovanni.carne@kit.edu)

Jaekeun Lee and Shenghui Cui are with the Department of Electrical and Computer Engineering and SNU Electric Power Research Institute, Seoul National University, 08826 Seoul, South Korea (e-mail: jaek709@snu.ac.kr; cuish@snu.ac.kr)

converters due to its simplicity [13], [14]. The SPS modulation adjusts only the load angles between multiple ports while maintaining duty cycles at 0.5, thereby maximizing the applied voltages to the transformer. This simplified control structure inherently enables zero-voltage switching (ZVS). However, this soft-switching capability of the SPS becomes limited under mismatched dc voltage ratios among the ports, particularly under light-load conditions. Furthermore, mismatches associated with the maximized voltages can induce excessive reactive currents, leading to further degradation of efficiency.

To address these limitations of the SPS, multi-variable modulation schemes with adjustable duty cycles can be employed for MAB3 converters. By adjusting duty cycles to compensate mismatched voltage ratios, these schemes can reduce reactive currents and extend the soft-switching range. However, in contrast to single-phase MAB converters, relatively few multi-variable modulations have been developed for MAB3 converters [15]–[17]. Nevertheless, developments of such modulation schemes for MAB3 converters are expected to grow, as indicated by emerging trends in foundational topologies. In both single-phase MAB converters [18]–[23] and three-phase DAB converters [24]–[28], the use of variable duty cycles has become increasingly prevalent. This trend highlights the strong potential of advancing multi-variable modulation schemes in MAB3 converters.

Despite this emerging potential, dynamic control methods that support multi-variable modulation for MAB3 converters remain underdeveloped. Without proper dynamic control method, abrupt variations in load angles and duty cycles can lead to overcurrent and flux saturation issues in the transformer, thereby limiting the power slew rate. To mitigate these issues, overdesign of transformer while keeping the high slew rate, or larger dc capacitance while lowering the slew rate can be employed. However, either way significantly degrades the power density benefit of MAB3 converter.

The existing dynamic control methods related to multi-variable modulation of MAB3 are listed on TABLE I. For the single-phase configuration, dynamic control methods that support multi-variable modulation schemes have been developed; [29] focused on winding current dynamics of the multi-winding transformer, while [30] considered both current and magnetizing flux-linkage dynamics. However, due to the different voltage patterns in the three-phase configuration, additional adaptations are needed for their application to MAB3 converters. Conversely,dynamic control methods focusing on the three-phase configuration have achieved transient current control [13], [14], or transient control of both current and magnetizing flux-linkage, [31]. However, their scope was limited to SPS modulation with fixed duty cycles.

Overall, the dynamic control of both current and magnetizing flux-linkage for multi-variable modulation of MAB3 converters is scarce. To address this gap, this article proposes an instantaneous pulse pattern control (IPPC) for MAB3 converters. The proposed IPPC can facilitate the application of various multi-variable modulation schemes to MAB3 converters, eliminating the need for the transformer overdesign or increased dc-link capacitance. Moreover, while the dynamic control method itself does not directly influence efficiency enhancement, it indirectly contributes to efficiency, by supporting the stable operation of multi-variable modulation with improved dynamic performance.

TABLE I
COMPARISON OF EXISTING AND PROPOSED DYNAMIC CONTROL METHODS FOR MAB CONVERTERS.

Methods	Control target	Topology	Variable duty cycle
[29]	Current	Single-phase	Yes
[30]	Current & flux	Single-phase	Yes
[13], [14]	Current	Three-phase	No
[31]	Current & flux	Three-phase	No
Proposed	Current & flux	Three-phase	Yes

A major challenge in the dynamic control of MAB3 is the complex dynamics of the multi-winding transformer, where all windings are mutually coupled through numerous inductance parameters. To address this, the IPPC leverages the straightforward dynamics of flux regulation, which exhibits inherently decoupled and independent to inductance parameters. By defining port-flux linkages as the time integral of applied voltages at each port, they can be estimated independently and regulated without transformer parameter dependency.

Additionally, the IPPC exploits the relationships between port-flux linkages, winding currents, and magnetizing flux-linkage. Both the winding current and the magnetizing flux-linkage can be expressed as linear combinations of port-flux linkages, as will be discussed in detail later. Therefore, by regulating multiple port flux-linkages into desired steady-state trajectories in accordance with modulation conditions such as load angle and duty cycles, the winding current and magnetizing flux-linkage can indirectly controlled while accommodating generic modulation schemes. Moreover, within this multi-flux regulation, a residual degree of freedom exists to distribute load angles over multiple ports. By exploiting this degree of freedom, the proposed IPPC consistently minimizes transient time, regardless of modulation conditions.

The multi-flux regulation structure in the proposed IPPC for MAB3 extends the dual-flux regulation structure, previously developed for dynamic control for DAB3 [32]–[34]. In contrast to these earlier methods, this article presents the following key contributions:

- A theoretical foundation that establishes relationships between port flux-linkages, winding currents and magnetizing flux-linkage of a three-phase multi-winding transformer.
- A generalization of multi-flux regulation framework accompanied with the load angle distribution scheme to multiport systems.
- Experimental validation of enhanced dynamic performance of the proposed IPPC under generic MAB3 modulation conditions.

The rest of this article is organized as follows. Section II presents dynamic modeling approaches for MAB3 converters, highlighting limitation of conventional control method and establishing the foundation to the proposed multi-flux regulation strategy. Section III proposes the IPPC for MAB3 converters, detailing the multi-flux regulation structure along with the load

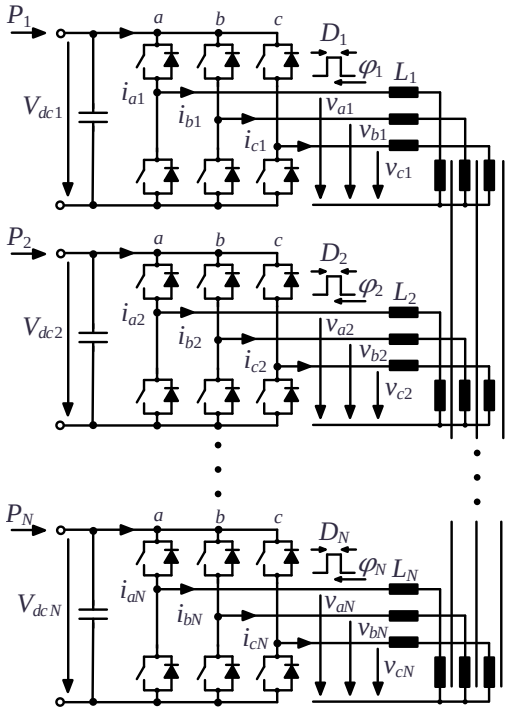

Fig. 2. Circuit diagram of the MAB3 converter.

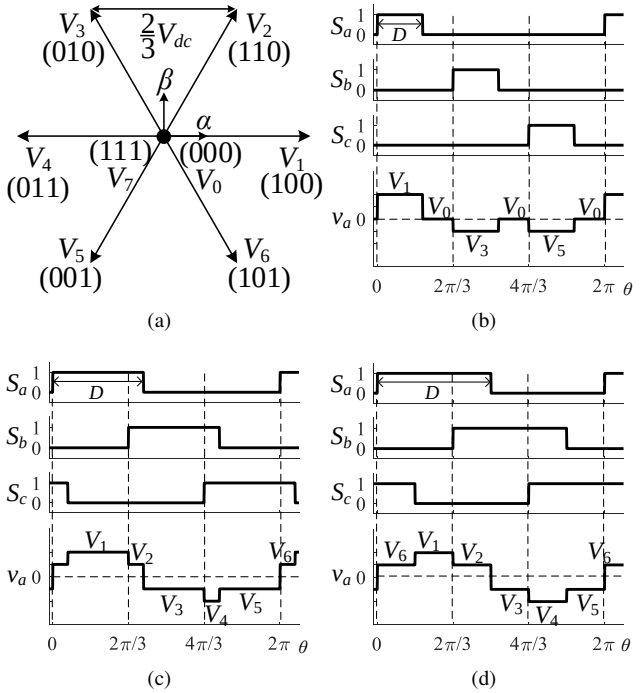

Fig. 3. (a) Voltage output vectors of each three-phase active bridge and voltage sequences according to the duty cycle: (b) $0 < D < \frac{1}{3}$, (c) $\frac{1}{3} < D < \frac{1}{2}$, and (d) $D = \frac{1}{2}$.

angle distribution scheme. Section IV experimentally validates the dynamic performance of the proposed IPPC under various modulation conditions. Finally, Section V summarizes and concludes this article.

II. Dynamic Modeling of MAB3 Converters

This section presents dynamic modeling approaches for MAB3 converters. The primary control objectives during dynamic regulation are the winding currents and the magnetizing flux-linkage of the multi-winding transformer. To effectively suppress overshoots and dc offsets in such targets, a dynamic model that captures the influence of applied voltages is essential. The first subsection revisits the conventional modeling approach for direct control, focusing on the direct effects of applied voltages on the winding currents and the magnetizing flux-linkage. The associated complexity and limitations of this approach are then discussed. To address these challenges, the second subsection introduces a novel modeling approach for indirect control. In the proposed modeling approach, the effects of applied voltages on winding currents and the magnetizing flux-linkage are port flux linkages as intermediate variables. This formulation offers a simplified and decoupled representation of multi-winding transformer, thereby enabling straightforward indirect control compatible with generic modulation schemes.

A. Conventional Modeling Approach for Direct Control

The MAB3 converter comprises multiple three-phase active bridges interconnected through a three-phase multi-winding transformer, as illustrated in Fig. 2. The pulse pattern of each active bridge can be characterized by its duty cycle, D_j, and port phase angle φ_j, Accordingly, an N-port MAB3 can adjust N duty cycles and N phase angles, resulting in a total of $2N$ variables. However, power flow is determined by the phase differences between the phase angles rather than the individual values of them. Therefore, the modulation of the MAB3 possesses $(2N-1)$ degrees of freedom and determines N duty cycles, and $(N-1)$ load angles according to the desired power flow.

The duty cycle of each three-phase active bridge in the MAB converter affects the applied voltage pattern on the corresponding winding of the multi-winding transformer. Depending on switching states of the active bridge, its feasible instantaneous voltage outputs are expressed in the stationary α-β frame, as illustrated in Fig. 3(a). Except for zero voltage vectors, V_0 and V_7, all voltage vectors form regular hexagon with there magnitudes of 2/3 times their corresponding dc-link voltage.

According to the duty cycle in the active bridge, their sequences are changed, as illustrated in Fig.3. First, for the duty-cycles less than 1/3, V_1, V_3, and V_5 are sequentially synthesized with V_0 between them, as illustrated in Fig. 3(b). The duration of V_0 decreases as D increases until when it becomes 1/3. The both fundamental and rms magnitudes of the phase voltage increase in this range.

In contrast, for the duty cycle larger than 1/3, zero voltage vectors are not utilized. V_1, V_2, V_3, V_4, V_5, and V_6 are sequentially synthesized, as shown in Fig. 3(c). As there are no zero voltage vectors within this range, the rms value of phase voltage remains constant, while the fundamental magnitude increases. Consequently, as illustrated in Fig. 3 (d), the fundamental voltage magnitude is maximized with the six-

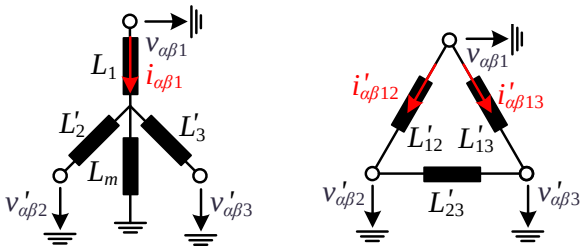

(a) (b)

Fig. 4. Exemplary equivalent circuits of MAB3 converter with three ports in the α-β stationary reference frame: (a) mesh connection and (b) star connection.

step waveform when D reaches 1/2, which is utilized as the fixed duty cycle in the SPS modulation. In summary, while the SPS modulation use only a single voltage pattern with the fixed duty cycle, multi-variable modulation uses various phase voltage patterns by adjusting duty cycles.

To represent dynamics of winding currents and the magnetizing flux-linkage from these phase voltages, the equivalent circuits of the MAB3 converter in the α-β frame are employed, as illustrated in Fig. 4 [14]. In these equivalent circuits, negligible winding resistances were assumed, and $'$ represents the converted value in the reference of port 1.

First, by reflecting the physical structure of a multi-winding transformer, the MAB3 converter can be represented with the equivalent circuit in a star connection. as shown in Fig. 4(a). In this circuit, the magnetizing flux-linkage, $\lambda_{\alpha\beta m}$, is defined in terms of magnetizing inductance, L_m, as follows:

$$\lambda_{\alpha\beta m} = L_m \sum_{k=1}^{N} i'_{\alpha\beta j}. \tag{1}$$

Based on the circuit as in Fig. 4(a), voltage equation on each leakage inductance, L'_j, can be represented as:

$$L'_j \frac{di'_{\alpha\beta j}}{dt} = v'_{\alpha\beta j} - \frac{d\lambda_{\alpha\beta m}}{dt}. \tag{2}$$

By combining (1) and (2), the dynamics of the magnetizing flux-linkage can be derived as:

$$\frac{d\lambda_{\alpha\beta m}}{dt} = \left(\frac{1}{L_m} + \sum_{k=1}^{N} \frac{1}{L'_j} \right)^{-1} \sum_{k=1}^{N} \frac{v'_{\alpha\beta j}}{L'_j}. \tag{3}$$

Although the dynamics of the winding current can be derived by combining (2) and (3), it would be too complicated due to coupled terms among leakage and magnetizing inductances. Alternatively, this equivalent circuit can be transformed into the mesh-connected circuit as depicted in Fig. 4(b). In the assumption of magnetizing inductance far larger than leakage inductances, the virtual leakage inductances of the mesh-connected circuit, L'_{jk}, can be derived from the original leakage inductances of the star-connected circuit as follows [35]:

$$L'_{jk} = L'_j L'_k \sum_{n=1}^{N} \frac{1}{L'_n}. \tag{4}$$

In the mesh-connected circuit, the winding current of each node is only affected by applied voltages on both ends. Due to this independent structure, the winding current flowing from the j-th port to k-th port can be derived as:

$$i'_{\alpha\beta jk} = \int \frac{v'_{\alpha\beta j} - v'_{\alpha\beta k}}{L'_{jk}}\, dt. \tag{5}$$

Consequently, by superposing the currents flowing from j-th port to the other ports in the mesh-connected circuit, the original winding current in the star-connected circuit, $i'_{\alpha\beta j}$ can be derived as:

$$i'_{\alpha\beta j} = \sum_{k=1, k\neq j}^{N} i'_{\alpha\beta jk}. \tag{6}$$

For instance, for three port-system as illustrated in Fig. 4, $i_{\alpha\beta1}$ can be calculated by summing $i'_{\alpha\beta12}$ and $i'_{\alpha\beta13}$.

By combining (5) and (6), the dynamics of each winding current can be represented:

$$\frac{di'_{\alpha\beta j}}{dt} = \sum_{k=1, k\neq j}^{N} \frac{v'_{\alpha\beta j} - v'_{\alpha\beta k}}{L'_{jk}}. \tag{7}$$

Overall, the system dynamics of the magnetizing flux-linkage and winding currents can be directly represented in terms of control inputs as in (3) and (7), respectively. Existing studies on dynamic control of MAB3 converters have either partially or fully incorporated these dynamics [13], [14], [31]. Earlier works focused solely on the winding current dynamics [13], [14], while the more recent study incorporated the dynamics of both winding current and magnetizing flux-linkage [31]. However, despite the differing scopes, all of these method share a common limitation: they are restricted to the SPS modulation. As evident from (3) and (7), their dynamic equations are coupled across multiple ports and rely on various inductance parameters, making them difficult to be generalized to modulation schemes with variable duty cycles.

B. Proposed Modeling Approach for Indirect Control

To overcome these limitations, this article proposes a modeling approach based on port flux-linkages for indirect control. The port-flux linkage, $\lambda'_{\alpha\beta j}$, is defined as the total flux-linkage induced by the applied voltage at a given port, comprising both leakage and magnetizing components. By definition, its dynamics with respect to the applied voltage can be expressed as:

$$\frac{d\lambda'_{\alpha\beta j}}{dt} = v'_{\alpha\beta j}. \tag{8}$$

Note that this system equation is fully decoupled across multiple ports, and independent of any inductance parameters. The flux-linkage at the j-th port depends solely on the applied voltage on the corresponding transformer winding. Furthermore, this equation is expressed in a simple first-order differential form. Overall, regulating the port flux-linkages provides decoupled, parameter-independent, and simplified controllability.

By leveraging these advantages of port flux-linkage regulation, both multi-variable and SPS modulations can be

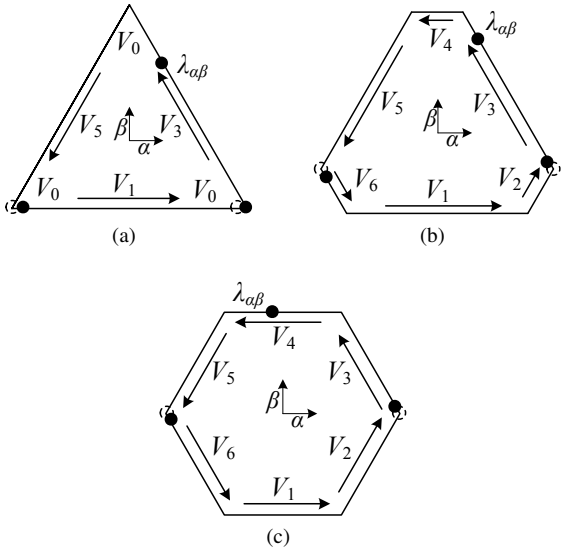

Fig. 5. Flux-linkage trajectories of an arbitrary port according to the duty cycle: (a) $0 < D < \frac{1}{3}$, (b) $\frac{1}{3} < D < \frac{1}{2}$, and (c) $D = \frac{1}{2}$.

effectively accommodated. Integrating both sides of (8), the port flux-linkage can be expressed as:

$$\lambda'_{\alpha\beta j} = \int v'_{\alpha\beta j} dt. \tag{9}$$

Based on this relationship, the steady-state trajectories of the port flux-linkage can be derived from the voltage sequences depicted in Fig. 3. For the duty cycles less than 1/3, V_1, V_3, and V_5 are sequentially applied, interleaved with V_0, resulting in the steady-state flux trajectory forming a regular triangle, as depicted in Fig. 5(a). For the duty cycles between 1/3 and 1/2, all six effective voltage vectors from V_1 to V_6 are applied with uneven durations, forming an asymmetrical hexagonal trajectory, as illustrated in Fig. 5(b). At a duty cycle of exactly 1/2, the fixed duty cycle under the SPS modulation, all six vectors are applied with equal durations, yielding the steady-state trajectory as a regular hexagon, as shown in Fig. 5(c).

Overall, SPS modulation forms a unique regular hexagonal trajectory of the port flux linkage, whereas the multi-variable modulation forms the various steady-state trajectories such as a regular triangle, an asymmetrical hexagon or a regular hexagon. Consequently, multi-flux regulation can seamlessly accommodate these modulation schemes by simply adjusting reference trajectories according to modulation conditions.

Concurrently, within the multi-flux regulation to handle the generic modulations, the magnetizing flux-linkage and winding currents can be controlled indirectly. By integrating both sides of (3), the magnetizing flux-linkage can be expressed as a linear combination of the port flux-linkages, as follows:

$$\begin{aligned} \lambda_{\alpha\beta m} &= \sum_{j=1}^{N} \alpha_j \lambda'_{\alpha\beta j}, \\ \alpha_j &= \left(\frac{1}{L_m} + \sum_{k=1}^{N} \frac{1}{L'_k} \right)^{-1} \frac{1}{L'_j}. \end{aligned} \tag{10}$$

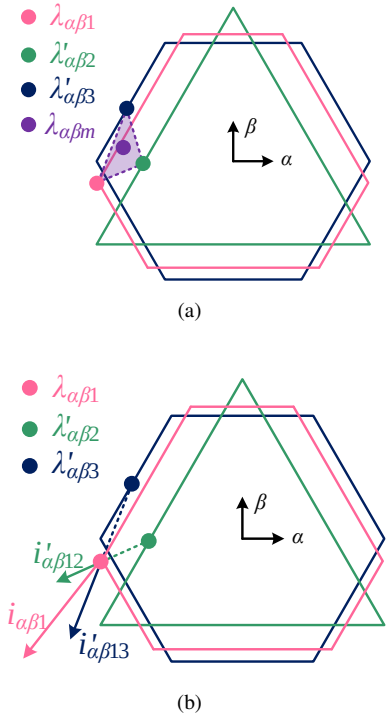

Fig. 6. Linear combination representations using port flux-linkages in an exemplary three-port MAB3 converter: (a) magnetizing flux-linkage and (b) winding currents.

Here, note that each coefficient, α_j, is positive, and the sum of all coefficients is less than unity as given by:

$$\sum_{j=1}^{N} \alpha_j = \left(\frac{1}{L_m} + \sum_{k=1}^{N} \frac{1}{L'_k} \right)^{-1} \sum_{j=1}^{N} \frac{1}{L'_j} < 1. \tag{11}$$

Consequently, the magnetizing and port flux-linkages can be represented in the α-β reference frame, as illustrated in Fig. 6(a). Due to these linear coefficients summing to less than unity, the magnetizing flux-linkage must be constrained within the polygon formed by port flux-linkages. For instance, in a three-port MAB3 converter, $\lambda_{\alpha\beta m}$ is constrained within the triangle defined by $\lambda_{\alpha\beta1}$, $\lambda'_{\alpha\beta2}$, and $\lambda'_{\alpha\beta3}$. Therefore, by regulating all the port flux-linkages within their permissible ranges, the magnetizing flux-linkage can also be indirectly constrained during transient state in a guaranteed manner.

Likewise, the winding currents can also be expressed in a linear combination of the port flux-linkages. By integrating both sides in (7), the winding currents can be represented as superpositions of port flux-linkage differences:

$$i'_{\alpha\beta j} = \sum_{k=1, k\neq j}^{N} \frac{\lambda'_{\alpha\beta j} - \lambda'_{\alpha\beta k}}{L'_{jk}}. \tag{12}$$

As illustrated in Fig. 6(b), each winding current in the α-β frame can be decomposed into individual components that are proportional to the differences between the port flux-linkages. For example, in a three-port MAB3 converter, $i'_{\alpha\beta1}$ can decomposed into $i'_{\alpha\beta12}$ and $i'_{\alpha\beta13}$, which are derived from $(\lambda_{\alpha\beta1} - \lambda'_{\alpha\beta2})$ and $(\lambda_{\alpha\beta1} - \lambda'_{\alpha\beta3})$, respectively. By regulating

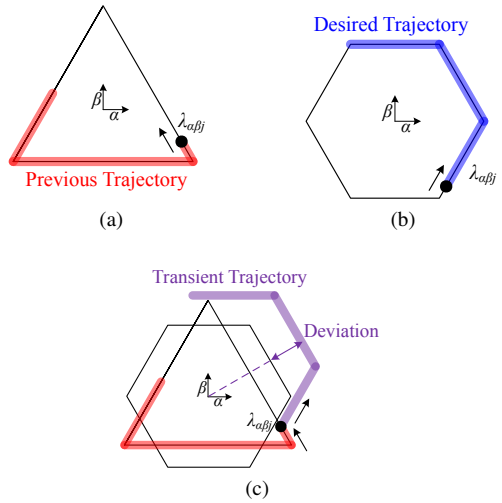

Fig. 7. Port flux trajectories in (a) the initial condition before transition, (b) the desired condition after transition, and (c) the transient state following an abrupt change of modulation conditions.

these port flux-linkages to follow balanced trajectories without dc offset and transient overshoot, the decomposed winding current components are also guaranteed to be controlled on balanced trajectories. Consequently, the overall winding currents, as their superpositions, remain balanced.

In summary, both the magnetizing flux-linkage and the winding currents can be expressed as linear combinations of port-flux-linkages. Based on this foundation regarding port-flux linkages, the current overshoots and flux offset during transient states can be analyzed. When the duty cycles and port-to-port angles are abruptly changed without dynamic control, the transient port flux trajectory becomes a composite of the previous and desired trajectories, as illustrated in Fig. 7. This arises from the voltage output synthesis assuming that the port-flux linkage is already following the desired steady-state trajectory. Consequently, a large deviation of the port flux-linkage from the origin occurs due to this trajectory mismatch. Finally, these deviations in port flux-linkages induce a transient offset in the magnetizing flux-linkage and overshoots in the winding currents, owing to the linear relationships relationships of port flux-linkages.

Conversely, these relationships—such as the sub-unity sum of the linear coefficients with the magnetizing flux-linkage and the definition of winding currents as superpositions of flux-differences—suggest that their transient control can be indirectly achieved through multi-flux regulation of port flux-linkages. Leveraging this insight, the following section proposes a dynamic control method based on multi-flux regulation structure to accommodate generic modulation schemes for MAB3 converters.

III. Proposed IPPC for MAB3 Converters

In this section, the instantaneous pulse pattern control (IPPC) is proposed as a generic dynamic control method to support both multi-variable and SPS modulations of MAB3

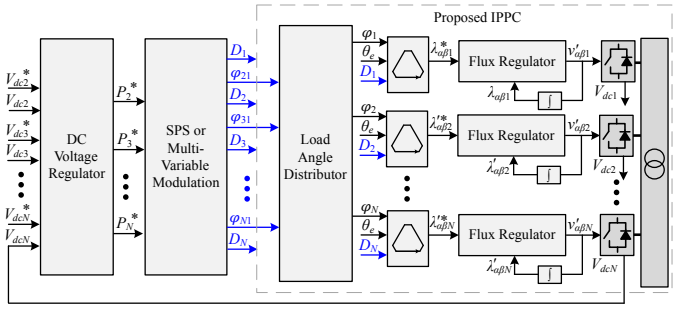

Fig. 8. Control scope of the proposed IPPC within an exemplary voltage regulation loop.

converters. Fig. 8 illustrates the control scope of the proposed IPPC within an exemplary voltage regulation loop. The outer voltage regulator determines the power flow setpoint of each port. In accordance with these setpoints, the modulation scheme determines the duty cycles and port-to-port load angles. Finally, the IPPC regulates the winding currents of the magnetizing flux-linkage to their corresponding steady state, based on these modulation variables.

The proposed IPPC consists of two major parts: a multi-flux regulation structure and load angle distribution scheme. By the multi-flux regulation of port flux-linkages toward these desired trajectories, the IPPC can accommodate generic modulation schemes. Simultaneously, by incorporating the load angle distribution scheme designed for enhanced dynamic performance, transient times can consistently minimized to a single sampling period, equivalent to one-sixth of the switching period.

Prior to detailing the multi-flux regulation structure and the load-angle distribution scheme, the following assumptions are established:

- Negligible voltage synthesis error: It is assumed that the dead time is significantly shorter than the switching period and that the winding resistance is negligible compared to the leakage inductance impedance. If voltage errors are non-negligible, they impose oscillatory responses on the flux linkages and winding currents, which are damped according to the time constants associated with the leakage inductance and winding resistance.
- Symmetrical leakage inductances: Symmetrical leakage inductances across the three phases are assumed. While the flux linkages may still converge as desired under asymmetric conditions, the corresponding winding currents will exhibit asymmetrical waveforms.
- Port number limitation: It is assumed that the port count is limited a maximum of four. For MAB3 converters exceeding four ports, the design of the three-phase multi-winding transformer becomes significantly more complex, and the computational burden increases accordingly.

A. Multi-Flux Regulation Structure

To leverage the straightforward controllability of port flux-linkages, the IPPC employs a multi-flux regulation structure, as illustrated in Fig. 8. Each flux regulation loop utilizes deadbeat control due to its simplicity. The dead beat flux

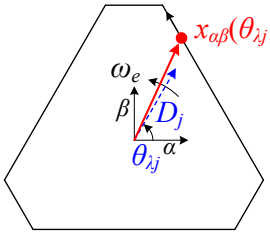

Fig. 9. Flux coordinate function in the α-β frame for the setpoint determination in each flux regulation loop.

regulator synthesizes the voltage output, $v'_{\alpha\beta j}[k]$, to directly shift the port flux-linkage, $\lambda'_{\alpha\beta j}[k]$, to its setpoint at the next step, $\lambda'^{*}_{\alpha\beta j}[k+1]$, within a sampling period, T_s, as:

$$v'_{\alpha\beta j}[k] = \frac{\lambda'^{*}_{\alpha\beta j}[k+1] - \lambda'_{\alpha\beta j}[k]}{T_s}. \tag{13}$$

As indicated by this equation, both the estimation of port flux-linkages and the derivation of their setpoints are required for the deadbeat flux control.

The port flux-linkage is estimated by integrating the previous applied voltage as:

$$\lambda'_{\alpha\beta j}[k] = \lambda'_{\alpha\beta j}[k-1] + T_s v'_{\alpha\beta j}[k-1]. \tag{14}$$

This approach eliminates the need for additional sensors to measure port flux-linkages. It aligns with the trend in model-based dynamic control methods on dc-dc converters based on medium-frequency transformers, which typically avoids high-bandwidth sensors for measuring winding currents or flux-linkages of the transformer [36], [37].

The setpoints for the port flux-linkages are derived based on the modulation conditions specified the upper-level control, including the N duty cycles, $(D_1, D_2, \ldots, D_N)$, and the $(N-1)$ port-to-port load angles, $(\varphi_{21}, \varphi_{31}, \ldots, \varphi_{N1})$. For this derivation, the relevant angular variables are defined as follows. For an arbitrary j-th port, port flux angle, $\theta_{\lambda j}$, is defined as the angle of the fundamental flux component with respect to the α-axis. This port flux angle consists of a synchronous angle, θ_e, and a port phase angle, φ_j as:

$$\theta_{\lambda j} = \theta_e + \varphi_j. \tag{15}$$

In this equation, the synchronous angle is a common component shared by all port flux angles. which is calculated in terms of the angular frequency, ω_e and the switching period, T_{sw} as:

$$\begin{aligned} \theta_e &:= \int \omega_e dt, \\ \omega_e &:= \frac{2\pi}{T_{sw}}. \end{aligned} \tag{16}$$

Subsequently, each port flux-linkage setpoint can be expressed using a flux coordinate function in the α-β reference frame, $x_{\alpha\beta}\ (\theta_{\lambda j}, D_j)$, as illustrated in Fig. 9. This function is derived from (9) based on the applied voltage sequences shown in Figs. 3 and 5. Since the voltage sequences for individual three-phase active bridges are identical in both DAB3 and MAB3 converters, the coordinate function, $x_{\alpha\beta}$, originally developed for DAB3 can be directly applied to MAB3. Accordingly, the IPPC employs $x_{\alpha\beta}(\theta_{\lambda j}, D_j)$, as derived in [32], and it is detailed in Appendix A. Overall, the setpoints of all port flux-linkages are expressed in terms of $x_{\alpha\beta}$ as:

$$^{\forall} j \in [1, N] \rightarrow \lambda'^{*}_{\alpha\beta j} = x_{\alpha\beta}(\theta_{\lambda j}, D_j). \tag{17}$$

These setpoints should satisfy the modulation condition imposed by port-to-port load angles as:

$$^{\forall} j \in [2, N-1] \rightarrow \theta_{\lambda j} - \theta_{\lambda 1} = \varphi_j - \varphi_1 = \varphi_{j1}. \tag{18}$$

Note that there is a single degree of freedom to set φ_1, since there are $(N-1)$ port-to-port load angles, whereas N port phase angles exist. Once φ_1 is determined as the baseline, all φ_{j1} are also consequently defined. Subsequently, all $\lambda^*_{\alpha\beta j}$ are determined, followed by the computation of $v_{\alpha\beta j}$ according to (13).

However, deadbeat control guarantees convergence within a single sampling period, only when the voltage output is not saturated [38], [39]. Consequently, the dynamic performance of flux regulation deteriorates when the voltage output of the deadbeat flux regulator is frequently saturated, as is the case in SPS modulation, which already fully utilizes maximized voltage magnitude. To address this limitation, the IPPC leverages the unique residual degree of freedom to set φ_1 for enhancing the dynamic performance of flux regulation. This degree of freedom is formulated as a load-angle distribution problem, which will be addressed in the subsequent subsection.

B. Proposed Load Angle Distribution Scheme

Dynamic performance degradation in deadbeat flux control is prone to occur during SPS modulation, since that modulation already utilizes the maximum available magnitude of the port voltage. As illustrated in Fig. 10(a), the feasible boundary of flux-linkage variation in one sampling period forms a hexagon. In the steady-state of SPS modulation, the maximized voltage magnitude is applied; therefore, the port flux-linkage moves to reach this boundary in every sampling period, tracing a hexagonal flux trajectory.

However, if the flux setpoint is changed to increase the port phase angle, the new setpoint may not be reachable within one sampling period. For example, as illustrated in Fig. 10(b), if the flux setpoint is changed at the first sampling instant to increase the phase angle, the new setpoint, $\lambda^*_{\alpha\beta j}[2]$, falls outside the reachable flux boundary. Consequently, due to voltage output saturation, the actual port flux-linkage, $\lambda_{\alpha\beta j}[2]$, is clamped by the hexagonal boundary, resulting in a tracking error. Since the subsequent flux setpoint, $\lambda^*_{\alpha\beta j}[3]$, follows the new steady-state trajectory of SPS modulation, this error persists over a prolonged transient time.

In contrast, if the flux setpoint is changed to decrease the port phase angle, the new setpoint is reachable within one sampling period. For example, as illustrated in Fig. 10(c), when the flux setpoint is changed at the first sampling instant to decrease the phase angle, the new setpoint, $\lambda^*_{\alpha\beta j}[2]$, lies within the hexagonal boundary. Subsequently, $\lambda^*_{\alpha\beta j}[3]$, becomes also reachable, allowing the port flux-linkage to converge into new

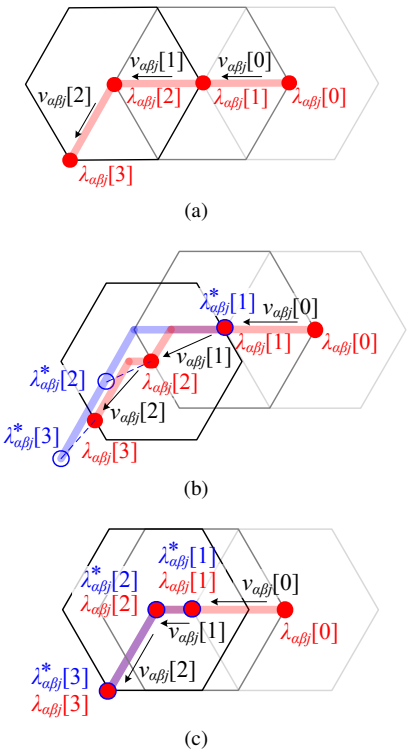

Fig. 10. Port flux trajectories: (a) steady state; (b) transient state under voltage output saturation; and (c) transient state with voltage output margin.

steady-state trajectory of SPS modulation, within a sampling period.

This dependence of dynamic performance on voltage output saturation can be effectively illustrated using an analogy of distance control between multiple vehicles driving at maximum speed. The relationship between the position and the velocity corresponds to that between the flux coordinate and the applied voltage. As previously mentioned, it is unfeasible to adjust the port-to-port angles among flux-linkages by increasing the voltage magnitude further under SPS modulation, since the magnitude of applied voltage is already at its maximum,. Similarly, when all vehicles are already at full speed, adjusting the distance between them through acceleration is not feasible. Therefore, alternative methods should be employed, as illustrated in Fig. 11.

One such approach involves taking an inner trajectory, as shown in Fig. 11(a). In this case, one vehicle can overtake others by maintaining full speed along a shorter path. Another approach is to apply braking to all vehicles except the target one, as illustrated in Fig. 11(b). This allows the target vehicle to advance while maintaining a full speed. Moreover, it effectively reduces the time required to adjust inter-vehicle distances by leveraging the greater available margin for speed reduction compared to acceleration. Therefore, whether increasing or decreasing the distance among multiple vehicles, applying brakes to the appropriate vehicle can minimize the time needed to achieve the desired distance.

Similarly, in port-to-port load angle control, there is greater flexibility in decreasing individual port phase angle than increasing it, due to the larger margin for reducing the magnitude of applied voltage. Therefore, the port-to-port load angle control that exclusively decreases individual port phase angle can minimize the transient time. To achieve this, a residual degree of freedom to set φ_1 can be utilized by formulating the equivalent problem in terms of the variations in port phase angle, $\Delta\varphi_j[k](:= \varphi_j[k] - \varphi_j[k-1])$, as follows:

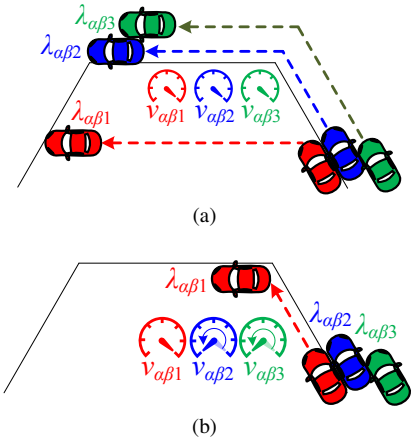

Fig. 11. Analogy of distance control between multiple vehicles at full speed: (a) utilization of an inner trajectory (b) utilization of braking.

$$\begin{aligned} &\text{Find} \quad \varphi_1[k] \\ \text{s.t.} \quad &{}^\forall j \in [2, N] \rightarrow \varphi_j[k] - \varphi_1[k] = \varphi_{j1}[k], \\ &\Delta\varphi_j[k] \leq 0. \end{aligned} \tag{19}$$

These inequality conditions can be reformulated as equality conditions using a function that finds the maximum of the given set as:

$$\begin{aligned} &\text{Find} \quad \varphi_1[k] \\ \text{s.t.} \quad &{}^\forall j \in [2, N] \rightarrow \varphi_j[k] - \varphi_1[k] = \varphi_{j1}[k], \\ &\max\left(\{\Delta\varphi_j[k]\}\right) = 0. \end{aligned} \tag{20}$$

Finally, the solution to distribute port-to-port load angles without any positive variations of port phase angles can be expressed as:

$$\begin{aligned} \Delta\varphi_1[k] &= -\max\left(\{\Delta\varphi_{j1}[k]\}\right), \\ \varphi_1[k] &= \Delta\varphi_1[k] + \varphi_1[k-1], \\ {}^\forall j \in [2, N] &\rightarrow \varphi_j = \varphi_{j1} + \varphi_1. \end{aligned} \tag{21}$$

Applying this solution to SPS modulation, the transient time can be effectively reduced even under using maximized voltage magnitudes induced from the fixed duty cycles. For multi-variable modulation, the proposed load angle distribution scheme remains effective, since the available voltage margin in the deadbeat flux regulator increases with reduced duty cycles.

Consequently, by applying the proposed load angle distribution scheme, the transient time can be effectively reduced to a single sampling period, regardless of modulation scheme. Within one sampling period, the variation in port-to-port load angle is bounded by:

$$\max\left(\{|\Delta\varphi_{j1}[k]|\}\right) \leq 2\omega_e T_s \tag{22}$$

This bound can also be explained with an analogy involving vehicles.: the maximum distance variation is achieved by driving vehicles at maximum speeds in opposite directions. Likewise, the maximum variation of port-to port load angle can be achieved by applying maximum voltages to change each port flux angles in opposite directions. In a typical digital signal processor (DSP)-based implementation, the sampling period is set to one-sixth of the switching period [32]. Thereby, max $(\{|\Delta\varphi_{j1}|\})$ is limited to 120° within a single sampling period. The practical range of load angles is typically constrained to [-60°, 60°] to avoid excessive reactive power. Therefore, it can be concluded that the proposed load angle distribution scheme can minimize the transient time to one-sixth of the switching period, regardless of modulation conditions.

In summary, given the N duty cycles and the $(N-1)$ port-to-port load angles from the upper-level modulation, the proposed load angle distribution scheme determines φ_1, following (21) to minimize transient time. Then the other port phase angles, $(\varphi_2, \varphi_3, ..., \varphi_N)$, are determined according to φ_1. With the determination of the N duty cycles and the N port phase angles, the N flux-reference trajectories are also determined, resulting in the derivation of the N voltage outputs through deadbeat flux regulators. Finally, these voltage outputs are converted into the desired switching patterns. By following this procedure, the IPPC achieves to minimize the transient times, regardless of modulation schemes. Since the conversion from voltage output to desired switching pattern in each individual three-phase active bridge is identical for both DAB3 and MAB3 converters, the IPPC adopts the switching pattern synthesis method originally developed for DAB3 [32].

IV. Experimental Validation

To validate the proposed IPPC for MAB3 converters, experimental tests were conducted using a prototype three-phase triple-active bridge (TAB3) converter, as illustrated in Fig. 12. The TAB3 prototype was constructed with a three-phase three-winding transformer was employing a ferrite core material N87 from TDK electronics, as illustrated in Fig. 12(a). Each three-phase active bridges was implemented with SiC MOSFETs and connected to the corresponding transformer winding, as illustrated in Fig. 12(b). The parameters of this TAB3 prototype with experimental conditions are summarized in TABLE II. To reflect the medium-frequency operation in high-power applications, the switching frequency was set to 5 kHz.

To evaluate the dynamic performance of power flow control, the step response of the proposed method was compared with that of the conventional method, which directly changes duty cycles and port-to-port load angles. For this step response observation, only the essential components were implemented, rather than employing the full configuration shown in Fig. 8. Instead of using a closed-loop voltage regulator, the power setpoint was manually changed in a step manner, while the respective dc voltages were regulated by external voltage supplies. Furthermore, the multi-variable modulation that converts power setpoints to modulation variables was implemented based on arbitrary combinations of duty cycles and port-to-port load angles, which satisfy the desired power flows.

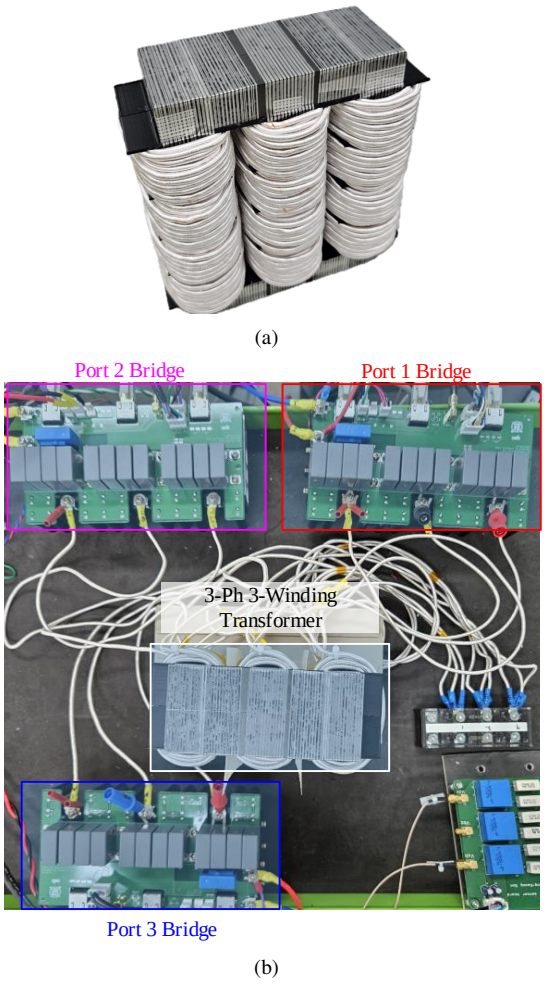

(a)

(b)

Fig. 12. Configuration of experimental setup: (a) three-phase three-winding transformer and (b) three-phase triple-active bridge (TAB3) converter.

TABLE II
Parameters of the TAB3 Prototype

Parameters	Port 1	Port 2	Port 3
Rated power [kW]	4	6	10
DC voltage [V]	160	240	400
Winding resistance [mΩ]	80	80	120
Winding turn ratio	1	1	2
Leakage inductance [μH]	50	50	100
Magnetizing inductance [mH]	2	-	-
Switching frequency [kHz]	5		
Sampling freqeunccy [kHz]	30		

These combinations of modulation variables for load condition sequences are listed in TABLE III.

The step responses of both methods under the load condition sequences defined in TABLE III for ports 1, 2 and 3 are shown in Figs. 13, 14, and 15, respectively. Each figure presents the three-phase port voltages, (v_{aj}, v_{bj}, v_{cj}), the three-phase winding currents (i_{aj}, i_{bj}, i_{cj}), and the dc voltage, v_{dcj}, for the respective port.

As illustrated in Figs. 13(a), 14(a), and 15(a), the conventional method exhibited prolonged transient responses for all

TABLE III
COMPARISON OF TRANSIENT TIMES BETWEEN THE CONVENTIONAL METHOD AND THE PROPOSED IPPC

Load condition	Idle	→ Light	→ Medium	→ Heavy	→ Idle
$[P_1^*, P_2^*, P_3^*]$ [kW]	$[0, 0, 0]$	$[0.8, 1.2, -2]$	$[2, 3, -5]$	$[4, 6, -10]$	$[0, 0, 0]$
$[D_1, D_2, D_3]$	$[0, 0, 0]$	$[0.306, 0.204, 0.245]$	$[0.340, 0.220, 0.264]$	$[0.5, 0.5, 0.5]$	$[0, 0, 0]$
$[\varphi_{21}, \varphi_{31}]$ [°]	$[0, 0]$	$[1.03, -9.73]$	$[2.82, -23.69]$	$[-0.02, -40.95]$	$[0, 0]$
ΔT_{conv} [μs]	-	800 $(= 4T_{sw})$	800 $(= 4T_{sw})$	1200 $(= 6T_{sw})$	1200 $(= 6T_{sw})$
ΔT_{prop} [μs]	-	33.3 $(= \frac{1}{6}T_{sw})$	33.3 $(= \frac{1}{6}T_{sw})$	33.3 $(= \frac{1}{6}T_{sw})$	33.3 $(= \frac{1}{6}T_{sw})$
Time reduction [%]	-	95.8	95.8	97.2	97.2

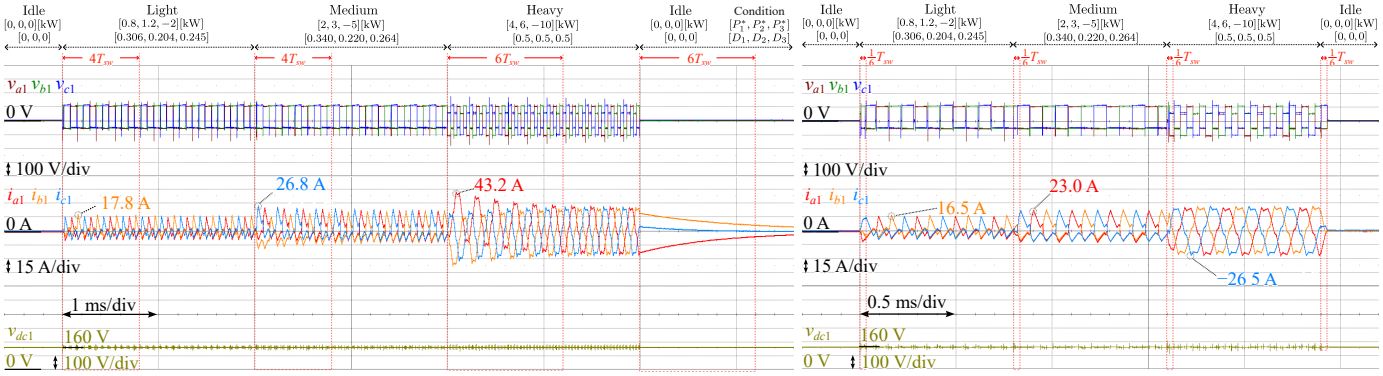

(a) (b)

Fig. 13. Step response of the port 1 under (a) the conventional method and (b) the proposed IPPC.

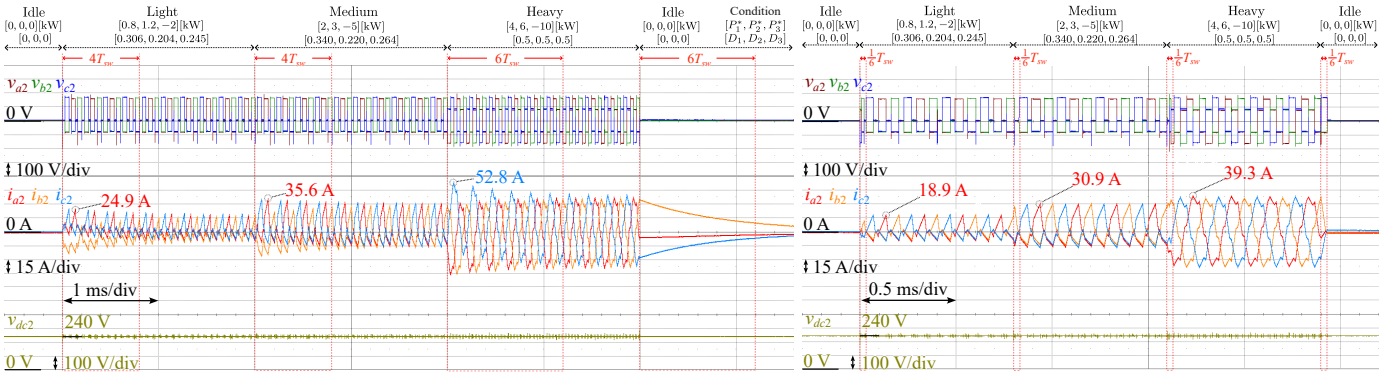

(a) (b)

Fig. 14. Step response of the port 2 under (a) the conventional method and (b) the proposed IPPC.

ports, accompanied by significant current overshoots. These overshoots were caused by the direct step changes in duty cycles and port-to-port load angles. Since the transients were naturally damped with a time constant determined by a ratio of leakage inductance to winding resistance, the low winding resistance led to extended settling times. Under sequential power variations, the measured transient times were 0.8 ms, 0.8 ms, 1.2 ms, and 1.2 ms, as listed in TABLE III. The most severe current overshoots occurred during the transition from the medium to heavy load conditions, when the modulation switched from multi-variable to SPS. The peak currents of ports 1,2 and 3 were 43.2 A, 52.8 A, and 38. 9 A, respectively.

In contrast, the proposed IPPC consistently minimized transient times without significant current overshoots, as illustrated in Figs. 13(b), 14(b), and 15(b). Compared to the conventional method, the proposed IPPC effectively reduced peak currents in the heavy load condition to -26.5 A, 39.3 A, and -29. 8 A for ports 1, 2, and 3, respectively. As a result, the proposed IPPC reduced these peak currents by 38.6 %, 28.6 %, and 23.3 %, thereby eliminating the necessity for transformer overdesign. Moreover, all transient durations were reduced to one-sixth of the switching period, corresponding to 33.3 μs, regardless of the modulation conditions. As summarized in TABLE III, the proposed IPPC reduced transient times by at least 95.8 % and up to 97.2 %, compared to the conventional method.

These advantages of the proposed IPPC stem from its multi-flux regulation structure accompanied with the load angle distribution scheme. The control behavior of this regulation

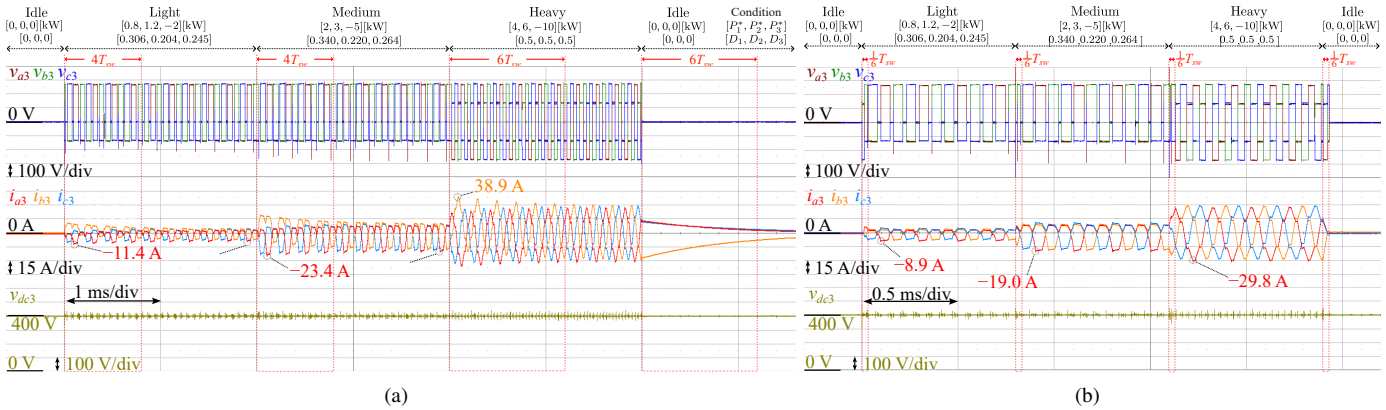

Fig. 15. Step response of the port 3 under (a) the conventional method and (b) the proposed IPPC.

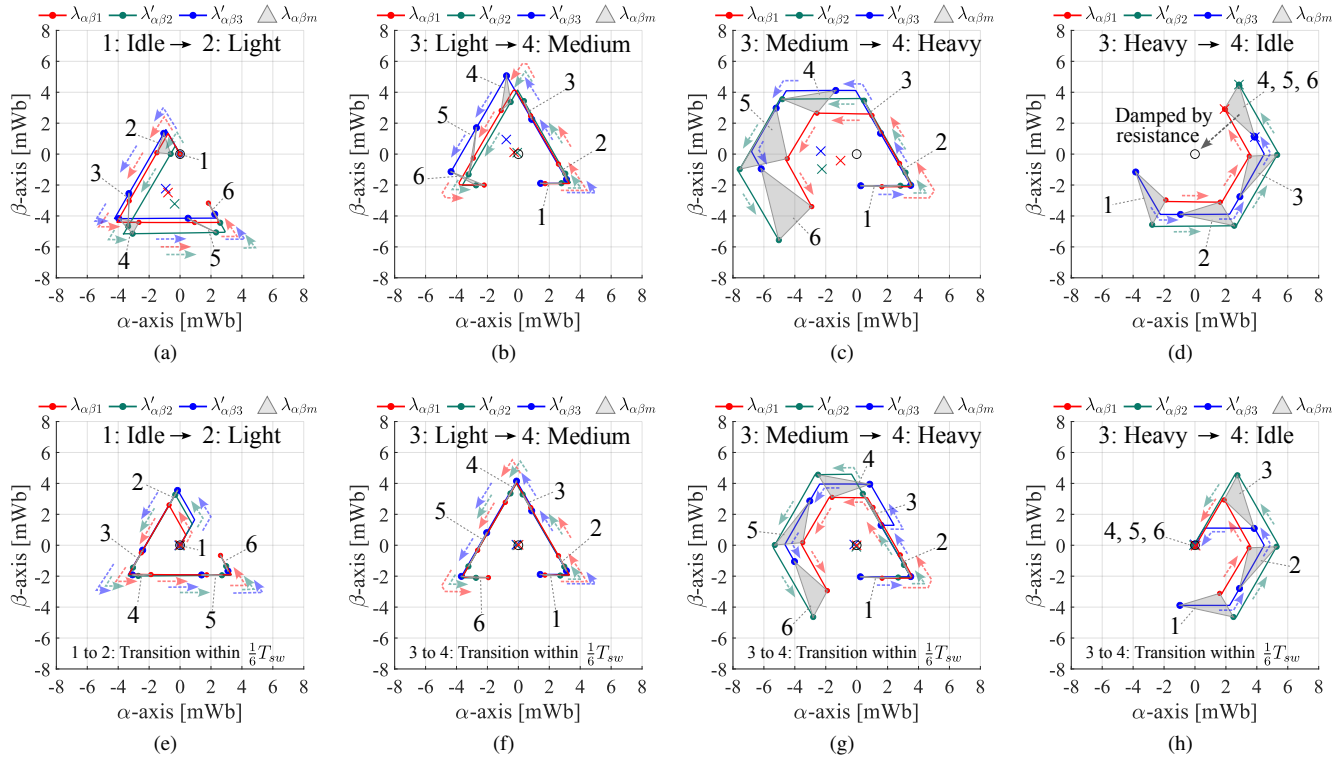

Fig. 16. Transient flux linkage trajectories under varying load conditions. (a)–(d): conventional method; (e)–(h) :the proposed IPPC. The transitions correspond to sequential load condition changes: (a), (e) idle → light load; (b), (f) light → medium load; (c), (g) medium → heavy load; and (d), (h) heavy → idle load.

method can be illustrated through the transient trajectories of flux-linkages in the α-β frame, as shown in Fig. 16. Each port flux-linkage was estimated by integrating the corresponding measured voltages. The transient trajectories were further characterized by flux-linkage coordinates captured at the sampling frequency, denoted as states 1 through 6 in each subplot. Additionally, the feasible region for the magnetizing flux-linkage was expressed by polygons, formed from the sampled coordinates of the port flux-linkages. The centroids of the port flux-linkages were marked with '×' symbols in colors corresponding to their respective trajectories.

As summarized in TABLE III, the duty cycles vary with different load conditions, resulting in distinct steady-state trajectories for each port flux-linkage. Regardless of the trajectory shape, their centroids should ideally remain at the origin. However, the conventional method induced dc offsets in the centroids of flux-linkage trajectories due to abrupt changes in duty cycles and port-to-port load angles.

As shown in Fig. 16(a), during the transition from idle to light load conditions, the centroids of all triangular trajectories deviated from the origin. Similarly, during the transition from light to medium load condition, the centroid of the port 3

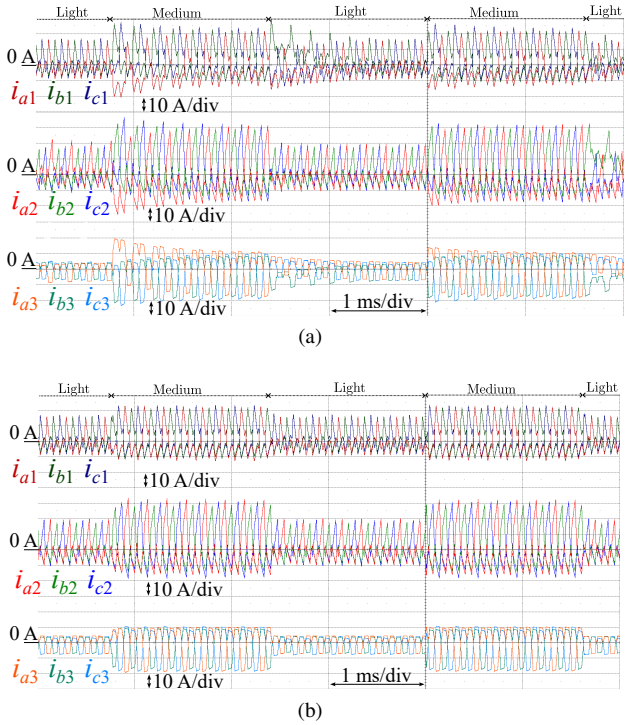

Fig. 17. Winding currents under periodic transitions between light and medium load conditions: (a) conventional method and (b) proposed method.

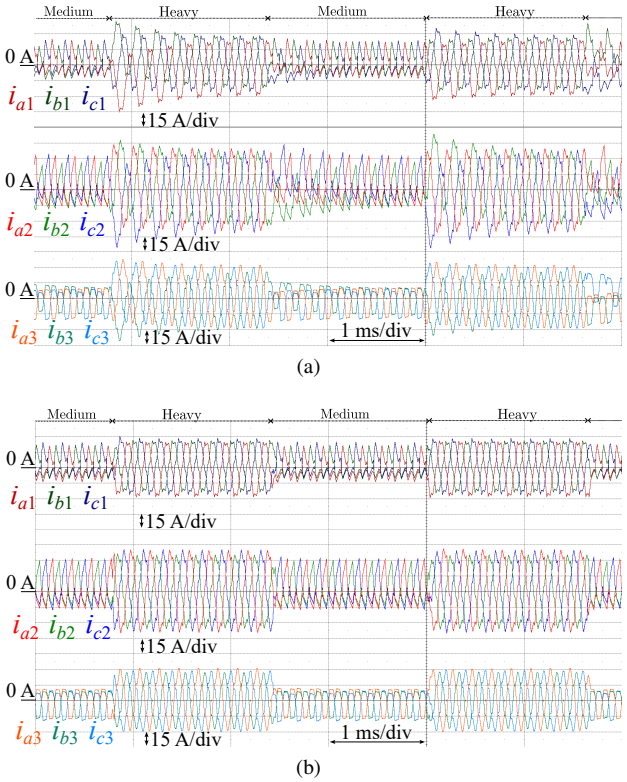

Fig. 18. Winding currents under periodic transitions between medium and heavy load conditions: (a) conventional method and (b) proposed method.

flux-linkage exhibited a significant deviation, as illustrated in Fig. 16(b). The most pronounced deviations occurred during the transition to heavy load condition, where the port flux linkage trajectories changed into hexagonal shapes for SPS modulation, as shown in Fig. 16(c). Finally, while returning to idle load condition, the flux-linkages remained stationary and failed to return to the origin, as shown in Fig. 16(d). These undesirable dc offsets not only increased the peak values of magnetizing flux-linkage but also amplified the differences among port flux-linkages, resulting in overshoots in the winding currents. Due to the low winding resistance, these dc offsets and overshoots were slowly damped, thereby prolonging the transient duration.

In contrast, the proposed method eliminated all transient dc offsets in the port flux-linkages, achieving transient times within a single sampling period, equivalent to 1/6 of the switching period. As shown in Figs. 16(e) and (h), by adjusting the reference trajectories of port flux-linkage between the desired shape and the origin, transitions to or from the idle load condition can be achieved within a single sampling period. Furthermore, as illustrated in Figs. 16(f) and (g), load angle distribution scheme, which exclusively decreases individual phase angle, facilitated rapid transitions. In both cases, since φ_{21} needed to increase, φ_1 and φ_3 were decreased while keeping φ_2 constant. As a result, all the port flux-linkages converged into the desired trajectories within a single sampling period, leading to the convergence of both the magnetizing flux-linkage and the winding currents, which are linear combinations of port flux-linkages.

The elimination of transient current overshoots and flux offset by the proposed IPPC can contribute to enhancing the efficiency of multi-variable under highly dynamic load conditions. Although efficiency primarily depends on steady-state modulation schemes, it can be influenced by the dynamic control method when the power flow changes frequently. For instance, power modulation strategies that periodically alternate between multiple operating points, such as time sharing control [5] or burst mode [40], can heighten the impact of dynamic control on the efficiency.

TABLE IV
EFFICIENCY COMPARISON UNDER HIGHLY DYNAMIC CONDITIONS

Load condition	Method	$[P_1, P_2, P_3]$ [kW]	η [%]
Light ↔ Medium	Conventional	[1.273, 2.044, -3.203]	97.40
	Proposed	[1.255, 2.027, -3.204]	97.62
Medium ↔ Heavy	Conventional	[2.734, 4.444, -6.911]	96.27
	Proposed	[2.703, 4.364,- 6.835]	96.72

To validate the efficiency enhancement provided by the proposed IPPC, the efficiency was measured by power analyzer Yokogawa WT5000 under highly dynamic load conditions and compared with the conventional method that abruptly changes duty cycles. The load conditions were alternated every 2 ms between two operating points for a total duration of 2 seconds. Fig. 17 shows the winding currents for both methods during periodic transitions between the light and medium load conditions, while Fig. 18 presents the transitions between the medium and heavy load conditions. The specific duty cycles and load angles for these conditions were applied according

to the values at TABLE. III.

As shown in Fig. 17(a) and Fig 18(a), the conventional method exhibited repetitive current overshoots, which induce higher conduction and switching losses. Since these current overshoots stem from differences between transient flux offsets, the repetitive offsets in the magnetizing flux-linkage also lead to increased core losses. In contrast, as shown in Fig. 17(b) and Fig 18(b), the proposed IPPC effectively eliminated repetitive current overshoots under highly dynamic load conditions. Consequently, as summarized in the TABLE IV, the proposed IPPC achieved an efficiency improvement of 0.22 %pt for the repetitive transitions between light and medium load conditions, and 0.52 %pt for the transitions between medium and heavy load conditions.

Overall, by leveraging the multi-flux regulation structure combined with the load angle distribution scheme, the proposed IPPC achieved transient control within minimal durations, regardless of the modulation conditions. This was accomplished without introducing overshoot in winding currents or transient flux-linkage offsets. As a result, the necessity for transformer overdesign or slew-rate limitation is effectively eliminated. Furthermore, the proposed IPPC enhanced the efficiency when using multi-variable modulation schemes under highly dynamic load conditions.

V. Conclusion

This article proposed the IPPC to facilitate the application of multi-variable modulation with improved dynamic performance. Due to complicated coupled nature of three-phase multi-winding transformer, the straightforward dynamics of port flux-linkages were employed.

It was theoretically demonstrated that the magnetizing flux-linkage is a linear combination of port flux-linkages, with the sum of coefficient being less than unity, and that the winding currents are superpositions of the differences between port flux-linkages. Based on these principles, a multi-flux regulation structure for the IPPC was formulated with the load angle distribution scheme. By regulating port flux-linkages into the corresponding steady-state trajectories, the generic modulation conditions can be accommodated. The load angle distribution scheme, which only decreases individual flux phase angles, effectively utilizes the available margin to reduce the applied voltage, enabling minimized transient times.

Experimental tests validated the proposed IPPC through comparisons with the conventional method that directly changes duty cycles and port-to-port load angles. In contrast to the conventional method, the proposed IPPC eliminated transient overshoots and dc offsets in the winding currents and magnetizing flux-linkage, achieving transitions within minimized transient times, regardless of modulation conditions. The prolonged transition times of the conventional method were reduced by at least 95.8 % and up to 97.2 % by the proposed IPPC.

Appendix A
Derivation of Flux-Linkage Coordinate Function

The port flux-linkage coordinate function, $x_{\alpha\beta}(\theta_{\lambda j}, D_j)$, can be derived as follows:

$$\begin{aligned} x_{\alpha\beta}\left(\theta_{\lambda j}, D_j\right) &= \mathbf{R}(\theta_c) z_{\alpha\beta}(r_\lambda, D_j), \\ \theta_c := \frac{2\pi}{3}m + \frac{\pi}{6} \quad &\text{s.t.} \quad |\theta_{\lambda j} - \theta_c| < \frac{\pi}{3}, \\ r_\lambda &:= \frac{3}{2\pi}(\theta_{\lambda j} - \theta_c). \end{aligned} \tag{23}$$

$$\begin{aligned} z_{\alpha\beta}\left(r_\lambda, D\right) &= \begin{bmatrix} z_\alpha(r_\lambda, r_c, h_1, h_2) \\ z_\beta(r_\lambda, r_c, h_1, h_2) \end{bmatrix}, \\ r_c &= \min\left(\frac{3D_j}{2}, 1 - \frac{3D_j}{2}\right), \\ h_1 &= \frac{4}{9} V_{dcj} r_c T_{sw}, \\ h_2 &= \frac{2}{3} V_{dcj}\left(\frac{D_j}{2} - \frac{r_c}{3}\right) r_c T_{sw}. \end{aligned} \tag{24}$$

$$\begin{aligned} &z_\alpha(r_\lambda, r_c, h_1, h_2) \\ &= \begin{cases} \dfrac{1}{\sqrt{3}}\left(\dfrac{h_1}{2} + h_2\right) & (|r_\lambda| \le r_c) \\ \dfrac{1}{\sqrt{3}}\left(\dfrac{h_1}{2} + h_2\right) - \dfrac{\sqrt{3}}{2} h_2 \dfrac{|r_\lambda| - r_c}{1 - 2r_c} & (|r_\lambda| > r_c) \end{cases}. \end{aligned} \tag{25}$$

$$\begin{aligned} &z_\beta(r_\lambda, r_c, h_1, h_2) \\ &= \begin{cases} \dfrac{h_1 r_\lambda}{2r_c} & (|r_\lambda| \le r_c) \\ \operatorname{sign}(r_\lambda)\left(\dfrac{h_1}{2} + \dfrac{1}{2} h_2 \dfrac{|r_\lambda| - r_c}{1 - 2r_c}\right) & (|r_\lambda| > r_c) \end{cases}. \end{aligned} \tag{26}$$

References

[1] C. Zhao, S. D. Round, and J. W. Kolar, "An isolated three-port bidirectional dc-dc converter with decoupled power flow management," *IEEE transactions on power electronics*, vol. 23, no. 5, pp. 2443–2453, 2008.

[2] M. Neubert, A. Gorodnichev, J. Gottschlich, and R. W. De Doncker, "Performance analysis of a triple-active bridge converter for interconnection of future dc-grids," in *2016 IEEE Energy Conversion Congress and Exposition (ECCE)*. IEEE, 2016, pp. 1–8.

[3] G. Buticchi, L. F. Costa, D. Barater, M. Liserre, and E. D. Amarillo, "A quadruple active bridge converter for the storage integration on the more electric aircraft," *IEEE Transactions on Power Electronics*, vol. 33, no. 9, pp. 8174–8186, 2017.

[4] L. F. Costa, G. Buticchi, and M. Liserre, "Optimum design of a multiple-active-bridge dc–dc converter for smart transformer," *IEEE Transactions on Power Electronics*, vol. 33, no. 12, pp. 10 112–10 121, 2018.

[5] Y. Chen, P. Wang, H. Li, and M. Chen, "Power flow control in multi-active-bridge converters: Theories and applications," in *2019 IEEE Applied Power Electronics Conference and Exposition (APEC)*. IEEE, 2019, pp. 1500–1507.

[6] J. Lee, J. Yun, H. Kim, and S. Cui, "High-fidelity fea-based circuit simulation for multi-active bridge converter," in *2024 IEEE Energy Conversion Congress and Exposition (ECCE)*. IEEE, 2024, pp. 3765–3770.

[7] P. Dworakowski, A. Wilk, M. Michna, B. Lefebvre, and T. Lagier, "3-phase medium frequency transformer for a 100kw 1.2 kv 20khz dual active bridge converter," in *IECON 2019-45th Annual Conference of the IEEE Industrial Electronics Society*, vol. 1. IEEE, 2019, pp. 4071–4076.

[8] H. van Hoek, M. Neubert, A. Kroeber, and R. W. De Doncker, "Comparison of a single-phase and a three-phase dual active bridge with low-voltage, high-current output," in *2012 International Conference on Renewable Energy Research and Applications (ICRERA)*. IEEE, 2012, pp. 1–6.

[9] N. H. Baars, J. Everts, C. G. Wijnands, and E. A. Lomonova, "Performance evaluation of a three-phase dual active bridge dc–dc converter with different transformer winding configurations," *IEEE Transactions on Power Electronics*, vol. 31, no. 10, pp. 6814–6823, 2015.

[10] J. Xue, F. Wang, D. Boroyevich, and Z. Shen, "Single-phase vs. three-phase high density power transformers," in *2010 IEEE Energy Conversion Congress and Exposition*. IEEE, 2010, pp. 4368–4375.

[11] T. Jimichi, M. Kaymak, and R. W. De Doncker, "Comparison of single-phase and three-phase dual-active bridge dc-dc converters with various semiconductor devices for offshore wind turbines," in *2017 IEEE 3rd International Future Energy Electronics Conference and ECCE Asia (IFEEC 2017-ECCE Asia)*. IEEE, 2017, pp. 591–596.

[12] U. Mustafa, I. Kougioulis, A. J. Watson, P. Wheeler, and M. R. Ahmed, "Design analysis of high-frequency, high power 3-phase dab transformer for electric vehicle charger applications," in *2024 IEEE Transportation Electrification Conference and Expo (ITEC)*. IEEE, 2024, pp. 1–6.

[13] M. Neubert, S. P. Engel, J. Gottschlich, and R. W. De Doncker, "Dynamic power control of three-phase multiport active bridge dc-dc converters for interconnection of future dc-grids," in *2017 IEEE 12th International Conference on Power Electronics and Drive Systems (PEDS)*. IEEE, 2017, pp. 639–646.

[14] M. Neubert, "Modeling, synthesis and operation of multiport-active bridge converters," Ph.D. dissertation, Dissertation, Rheinisch-Westfälische Technische Hochschule Aachen, 2020.

[15] M. Neubert, H. van Hoek, J. Gottschlich, and R. W. De Doncker, "Soft-switching operation strategy for three-phase multiport-active bridge dc-dc converters," in *2017 IEEE 12th International Conference on Power Electronics and Drive Systems (PEDS)*. IEEE, 2017, pp. 1–207.

[16] A. Thönnessen, C. Fronczek, and R. W. De Doncker, "Duty-cycle control of three-phase multi-active-bridge converters," *IEEE Journal of Emerging and Selected Topics in Power Electronics*, 2025.

[17] J. Yun, "Modulation scheme and dynamic control for improved light-load operation of three-phase multi-active bridge converter," Ph.D. dissertation, Seoul National University Graduate School, 2024.

[18] C. Zhao, "Isolated three-port bidirectional dc-dc converter," Ph.D. dissertation, ETH Zurich, 2010.

[19] R. Yapa and A. Forsyth, "Extended soft switching operation of the triple active bridge converter," in *6th IET International Conference on Power Electronics, Machines and Drives (PEMD 2012)*. IET, 2012, pp. 1–6.

[20] J. Li, Q. Luo, T. Luo, D. Mou, and M. Liserre, "Efficiency optimization scheme for isolated triple active bridge dc–dc converter with full soft-switching and minimized rms current," *IEEE Transactions on Power Electronics*, vol. 37, no. 8, pp. 9114–9128, 2022.

[21] S. Dey and A. Mallik, "Multivariable-modulation-based conduction loss minimization in a triple-active-bridge converter," *IEEE Transactions on Power Electronics*, vol. 37, no. 6, pp. 6599–6612, 2022.

[22] A. A. Ibrahim, A. Zilio, T. Younis, D. Biadene, T. Caldognetto, and P. Mattavelli, "Optimal modulation of triple active bridge converters by an artificial-neural-network approach," *IEEE Transactions on Industrial Electronics*, vol. 71, no. 3, pp. 2590–2600, 2023.

[23] C. Gao, K. Li, Z. Zhang, S. Zhang, S. Zhang, X. You, and S. Lu, "Generalized model of n-port modular multi-active-bridge converter with multiple-phase-shift modulation," *IEEE Transactions on Transportation Electrification*, 2024.

[24] H. van Hoek, M. Neubert, and R. W. De Doncker, "Enhanced modulation strategy for a three-phase dual active bridge—boosting efficiency of an electric vehicle converter," *IEEE Transactions on Power Electronics*, vol. 28, no. 12, pp. 5499–5507, 2013.

[25] J. Huang, Z. Li, L. Shi, Y. Wang, and J. Zhu, "Optimized modulation and dynamic control of a three-phase dual active bridge converter with variable duty cycles," *IEEE Transactions on Power Electronics*, vol. 34, no. 3, pp. 2856–2873, 2018.

[26] L. M. Cúnico, Z. M. Alves, and A. L. Kirsten, "Efficiency-optimized modulation scheme for three-phase dual-active-bridge dc–dc converter," *IEEE Transactions on Industrial Electronics*, vol. 68, no. 7, pp. 5955–5965, 2020.

[27] J. Hu, Z. Yang, S. Cui, and R. W. De Doncker, "Closed-form asymmetrical duty-cycle control to extend the soft-switching range of three-phase dual-active-bridge converters," *IEEE Transactions on Power Electronics*, vol. 36, no. 8, pp. 9609–9622, 2021.

[28] J. Yun and S. Cui, "Enhanced active thermal balancing strategy for three-phase dual-active bridge converter suppressing transformer flux saturation," *IEEE Transactions on Power Electronics*, 2024.

[29] S. Wei, D. Mou, W. Wen, Z. Zhao, and K. Li, "Transient dc bias and universal dynamic modulation of multiactive bridge converters," *IEEE Transactions on Power Electronics*, vol. 37, no. 10, pp. 11 516–11 522, 2022.

[30] J. Hu, S. Cui, and Y. He, "Universal flux balancing control to suppress transient dc-bias of phase-shift modulated multi-active-bridge converters," in *2023 11th International Conference on Power Electronics and ECCE Asia (ICPE 2023-ECCE Asia)*. IEEE, 2023, pp. 1898–1905.

[31] A. Thönnessen, C. Fronczek, and R. W. De Doncker, "Instantaneous flux and current control for three-phase multi-active-bridge dc-dc converters," in *2023 25th European Conference on Power Electronics and Applications (EPE'23 ECCE Europe)*. IEEE, 2023, pp. 1–8.

[32] J. Yun, S. Cui, and S.-K. Sul, "Instantaneous pulse pattern control for optimized dynamic performance of three-phase dual-active bridge converter," *IEEE Transactions on Power Electronics*, 2025.

[33] J. Yun, S. Cui, and S.-K. Sul, "Instantaneous dual flux control for three-phase dual-active bridge," in *2023 IEEE Energy Conversion Congress and Exposition (ECCE)*. IEEE, 2023, pp. 2747–2751.

[34] J. Yun, S. Cui, and S.-K. Sul, "Generalized instantaneous dual flux control for three-phase dual-active bridge converter," in *2024 IEEE Applied Power Electronics Conference and Exposition (APEC)*. IEEE, 2024, pp. 440–444.

[35] E. Wilkinson, "Mesh/star and star/mesh conversions," *IEEE Transactions on Education*, vol. 10, no. 2, pp. 103–105, 2007.

[36] S. P. Engel, N. Soltau, H. Stagge, and R. W. De Doncker, "Dynamic and balanced control of three-phase high-power dual-active bridge dc–dc converters in dc-grid applications," *IEEE Transactions on Power Electronics*, vol. 28, no. 4, pp. 1880–1889, 2012.

[37] J. Hu, "Modulation and dynamic control of intelligent dual-active-bridge converter based substations for flexible dc grids," Ph.D. dissertation, Dissertation, RWTH Aachen University, 2019.

[38] M. S. Petit, B. Sarlioglu, R. D. Lorenz, B. S. Gagas, and C. W. Secrest, "Deadbeat flux vector control for dynamic six-step operation of synchronous machines," in *2019 IEEE Transportation Electrification Conference and Expo (ITEC)*. IEEE, 2019, pp. 1–6.

[39] J. Yun, J. Yoo, S. Cui, and S.-K. Sul, "Model predictive control for six-step operation of pmsm based on adapted fast gradient method," *IEEE Trans. on Power Elec.*, vol. 38, no. 5, pp. 5952–5962, 2023.

[40] G. G. Oggier and M. Ordonez, "High-efficiency dab converter using switching sequences and burst mode," *IEEE Transactions on Power Electronics*, vol. 31, no. 3, pp. 2069–2082, 2015.